Parallel electron heating in the magnetospheric inflow region

Shan Wang, Li-Jen Chen, Michael Hesse, Lynn B. Wilson, Naoki Bessho, Daniel J. Gershman, Robert E. Ergun, Tai D. Phan, James L. Burch, John C. Dorelli, et al.

AGU PUBLICATIONS

Geophysical Research Letters

RESEARCH LETTER
10.1002/2017GL073404

Key Points:
- A sublayer in the magnetospheric inflow with decreasing $T_{e\|}$ and increasing density toward the separatrix is shown to be a common feature
- Penetration of fresh magnetosheath electrons may partially account for the $T_{e\|}$ decrease and density increase toward the separatrix
- High-energy electron phase-space density variations in magnetosphere inflow are collocated with waves in the lower hybrid frequency range

Correspondence to:
S. Wang,
swang90@umd.edu

Citation:
Wang, S., et al. (2017), Parallel electron heating in the magnetospheric inflow region, *Geophys. Res. Lett.*, *44*, 4384–4392, doi:10.1002/2017GL073404.

Received 10 MAR 2017
Accepted 3 MAY 2017
Accepted article online 8 MAY 2017
Published online 21 MAY 2017

Parallel electron heating in the magnetospheric inflow region

Shan Wang[1,2], Li-Jen Chen[1,2], Michael Hesse[3], Lynn B. Wilson III[2], Naoki Bessho[1,2], Daniel J. Gershman[2], Robert E. Ergun[4], Tai D. Phan[5], James L. Burch[6], John C. Dorelli[2], Barbara Giles[2], Roy B. Torbert[7], Craig J. Pollock[8], Christopher T. Russell[9], Robert Strangeway[9], Levon Avanov[2], Benoit Lavraud[10,11], and Thomas E. Moore[2]

[1]Astronomy Department, University of Maryland, College Park, Maryland, USA, [2]NASA Goddard Space Flight Center, Greenbelt, Maryland, USA, [3]Department of Physics and Technology, University of Bergen, Bergen, Norway, [4]Laboratory for Atmospheric and Space Physics, University of Colorado Boulder, Boulder, Colorado, USA, [5]Space Sciences Laboratory, University of California, Berkeley, California, USA, [6]Space Science and Engineering Division, Southwest Research Institute San Antonio, San Antonio, Texas, USA, [7]Space Science Center, University of New Hampshire, Durham, New Hampshire, USA, [8]Denali Scientific LLC, Healy, Alaska, USA, [9]Department of Earth, Planetary, and Space Sciences, University of California, Los Angeles, California, USA, [10]Institut de Recherche en Astrophysique et Planétologie, Université de Toulouse, Toulouse, France, [11]Centre National de la Recherche Scientifique, UMR 5277, Toulouse, France

Abstract We analyzed 20 reconnection events observed by the Magnetosphere MultiScale mission, finding that in a subregion of the magnetospheric inflow, the electron temperature parallel to the magnetic field ($T_{e\|}$) decreases toward the separatrix with increasing densities. Such $T_{e\|}$ variation is not consistent with the heating through the parallel potential mechanism for magnetospheric electrons. Associated with the change in $T_{e\|}$, low-energy gyrotropic magnetosheath-like electrons are observed. These electrons may come from the magnetosheath, penetrate to the magnetospheric side possibly due to waves in the lower hybrid frequency range, and do not experience as much energization as those from deeper in the magnetosphere. In addition, as $T_{e\|}$ decreases, the high-energy field-aligned phase-space densities decrease or fluctuate significantly over time. Wave-particle interaction might produce energy conversion and cause the high-energy phase-space density variations.

1. Introduction

Magnetic reconnection is an important mechanism for plasma transport and energization. Electrons and ions from two sides of the inflow region mix in the outflow region, and the magnetic energy is partially converted to plasma kinetic energies. Heating of electrons starts from the reconnection inflow region, i.e., on not yet reconnected magnetic field lines [*Chen et al.*, 2008], and will influence energization and pitch angle scattering in the exhaust [e.g., *Egedal et al.*, 2009; *Bessho et al.*, 2015; *Lavraud et al.*, 2016].

Inside the ion diffusion region in asymmetric reconnection, electrons moving in the inflow region follow magnetic moment (μ) conservation and are accelerated by the parallel potential ($\Phi_{\|}$) toward the reconnection site, where $\Phi_{\|}$ is the integral of $E_{\|}$ along the magnetic field to infinity [*Egedal et al.*, 2011]. *Le et al.* [2009] derived electron distributions in the reconnection region according to Liouville's theorem for symmetric reconnection. The resulting field-aligned electron distribution has a flat-top-like shape with constant phase-space densities (f) below the shoulder energy equal to $e\Phi_{\|}$, where $-e$ is the electron charge [*Egedal et al.*, 2010]. Based on the derived distributions, the electron parallel temperature in the inflow region follows the scaling law:

$$T_{e\|} \propto n^2/B^2 \tag{1}$$

where n is density and B is the magnetic field strength. The scaling law has been shown to apply in the magnetospheric inflow region during asymmetric reconnection for two-dimensional (2-D) particle-in-cell (PIC) simulations, and $T_{e\|}$ as well as n of magnetospheric origin inflow electrons increases toward the current sheet [*Egedal et al.*, 2011]. The electron density enhancement near the reconnection site inside the ion diffusion region is associated with drawing in magnetospheric electrons along magnetic fields

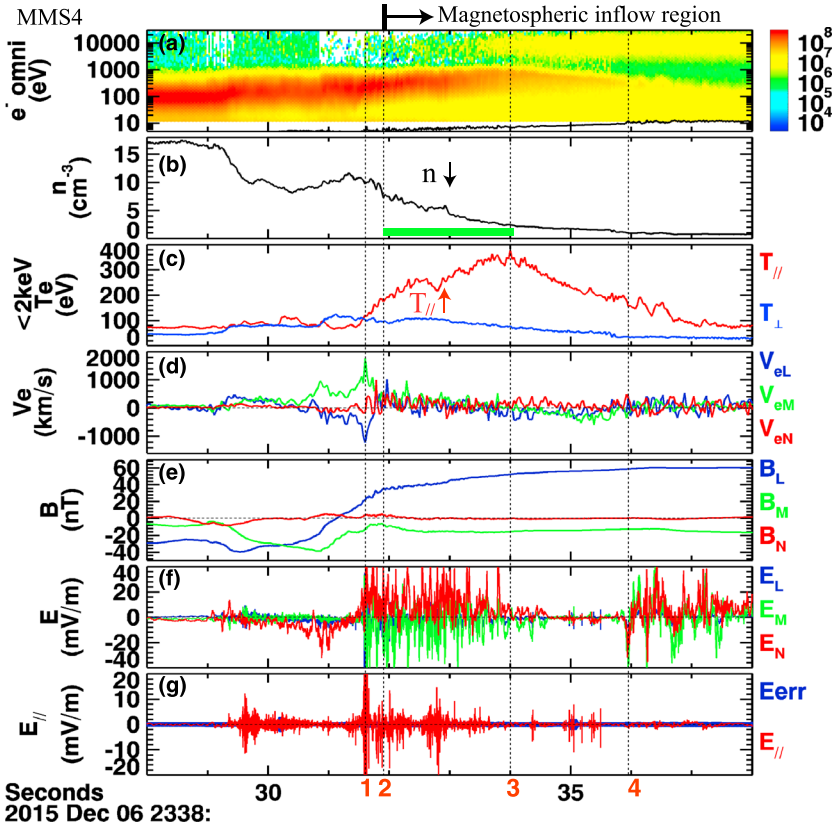

Figure 1. MMS4 crossing of the parallel electron heating region in the magnetopsheric side inflow that cannot be explained by the typical parallel potential alone (marked by the green bar), on 6 December 2015. (a) Omni-directional electron energy flux overplotted with the spacecraft potential (black). In the marked interval, (b) the electron density decreases, while (c) the parallel electron temperature for <2 keV populations increases. (d) The peak (location 1) to the end (location 2) of the electron bulk flow is close to the separatrix. (e) Magnetic field. (f) Electric field with much fluctuation in the marked interval. (j) Parallel electric field (red) and its uncertainty (blue). The vertical dashed lines 2–4 mark the time for electron distributions shown in Figure 2.

and is needed to maintain the charge neutrality as magnetosheath ions penetrate deeper to the magnetospheric inflow region than electrons due to the finite gyroradius effect [*Shay et al.*, 2016; *Phan et al.*, 2016].

The Magnetosphere MultiScale (MMS) observation shown in this paper examines whether the parallel potential mechanism for magnetospheric electrons alone explains the electron heating in the magnetospheric inflow region. We will show that in a sublayer close to the separatrix, $T_{e\|}$ decreases with increasing density toward the separatrix, in contrast with that predicted by *Egedal et al.* [2011]. Our work provides observation constraints on the heating mechanism(s) for magnetospheric inflow electrons.

2. Data

The observations are from the Magnetosphere MultiScale (MMS) burst-mode measurements. Electron data are from Dual Electron Spectrometers (DES) onboard Fast Plasma Investigation (FPI) package for an energy range of 10 eV to 30 keV, with 30 ms time resolution [*Pollock et al.*, 2016]. The 128 samples/s magnetic fields are taken from FluxGate Magnetometers [*Russell et al.*, 2016]. The 8192 samples/s electric fields are from axial and spin-plane double-probe field sensors [*Torbert et al.*, 2014]. The analysis uses the *LMN* coordinate system, where *L* is along the outflow direction, pointing toward the reconnecting magnetic field on the magnetospheric side; *N* is normal to the current sheet toward the magnetosheath; and *M* finishes the right-handed *LMN* coordinate.

3. Observations

3.1. Event on 6 December 2015

We first analyze the parallel electron heating in a reconnection event observed by MMS on 6 December 2015, reported to be 1–2 ion inertial lengths (d_i) downstream of the X line by *Khotyaintsev et al.* [2016]. The spacecraft moved from the magnetosheath to the magnetosphere (Figure 1). Near the end of the interval, relatively steady density (Figure 1b) and magnetic field (Figure 1e) are observed, which represent the magnetospheric upstream conditions of the reconnection. In this upstream region, the electron energy flux (Figure 1a) shows that in addition to high-energy ring current electrons above 2 keV, another population below ~200 eV exists. These low-energy electrons could be originally from the magnetosheath and were transported to the magnetospheric side during earlier or distant reconnection, acting as the magnetospheric inflow for the ongoing reconnection (e.g., discussed in *Le Contel et al*. [2016], *Graham et al.* [2016a], and *Phan et al.* [2016]). Around the magnetospheric inflow region between locations 1 and 4 (marked as red numbers at the bottom of the figure), the partial moment $T_{e||}$ of electrons with energies below 2 keV is higher than both inside the current sheet and upstream magnetosphere (Figure 1c). When calculating the temperature, the effect of the spacecraft potential (black curve overplotted in Figure 1a) is accounted for through subtracting the potential from electron energies. As n increases (Figure 1b) and B decreases (Figure 1e) from locations 4 to 1, $T_{e||}$ exhibits a peak at location 3 (23:38:34 UT) and decreases toward location 1 rather than monotonically increasing toward the separatrix, which appears to be inconsistent with the predicted scaling law $T_{e||} \propto n^2/B^2$(equation (1)). Below we analyze the electron heating regions (1–4) in more details. Electric fields (Figure 1f) and their parallel component (Figure 1g) exhibit significant fluctuations in the intervals 1–3, which will be discussed later.

The magnetospheric separatrix is close to the peak of the electron jet (Figure 1d) at location 1 [*Khotyaintsev et al.*, 2016]. Figure 2a shows the electron distribution at location 1 in the $v_{||} - v_{\perp 1}$ and $v_{\perp 1} - v_{\perp 2}$ planes cut at the bulk velocity in the third direction, where $v_{\perp 1}$ is along $\hat{b}\times\left(\hat{b}\times\hat{v}\right)$, $v_{\perp 2}$ is along $\hat{b}\times\hat{v}$, and $\hat{v}$ is the bulk velocity direction. The dotted lines mark the bulk velocities in each direction. Outflowing (mainly along L) magnetosheath electrons with high phase-space densities (f) have $v_{||} < 0$. The resulting distribution is nongyrotropic with asymmetry along $v_{\perp 1}$ relative to the bulk velocity, due to finite Larmor radius effects (either during meandering or magnetized gyration) close to their accessible magnetospheric boundary as well as acceleration by E_N [*Bessho et al.*, 2016; *Shay et al.*, 2016], which leads to large bulk V_M.

During the intervals 2–4, the spacecraft was in the magnetospheric inflow region, and no outflowing magnetosheath electrons with high f at $v_{||} < 0$ and nongyrotropic distributions exist. Figure 2b shows distributions at locations 2–4 with 1-D distributions along the parallel and antiparallel directions in Figure 2c. The 1-D distributions for each energy channel between 40 eV and 2 keV and their ratios ($f_{||+}/f_{||-}$ plotted in the logarithm scale) between the parallel and antiparallel directions are shown in Figures 2d–2f. Distributions shown in Figures 2b–2f are accumulated over five frames in time (0.15 s) to reduce the statistical uncertainties (overplotted as errorbars on the data points in Figure 2c). Energies are subtracted by the average spacecraft potential during the accumulation time, and distributions are interpolated to the energy channels before the spacecraft potential correction to create Figures 2d–2f. The black curve overplotted in Figure 2f is $T_{e||}$ for $<$2 keV electrons. From locations 2 to 4, distributions are gyrotropic, and balanced distributions between the parallel and antiparallel directions (the ratio $f_{||+}/f_{||-}$ is close to unity; Figure 2f) support that the spacecraft was in the inflow region.

The evolution of the distributions suggests that the $T_{e||}$ variation during the intervals 2–4 is due to both mixing and energization/cooling. Figure 2c shows that the distribution above ~30 eV at location 2 has a flat shape with shoulder energies where f has a sharp fall-off (around 200 eV). Distributions at locations 3 and 4 have decreasing slopes above ~30 eV and also have shoulder energies around 900 eV and 300 eV, respectively. The f below 30 eV may contain the photoelectrons induced by DES instruments, so we focus our discussion on electrons above 30 eV. Particles are expected to convect with the magnetic fields toward the current sheet; therefore, we will discuss in order from locations 4 to 2.

From locations 4 to 3 with increasing densities, high-energy f (above ~500 eV, close to and above shoulder energies) as well as shoulder energies increases, as shown in Figures 2c–2e (the blue arrows in Figure 2e illustrate this trend). Low-energy f (below 300 eV, green and yellow curves) at each energy channel roughly

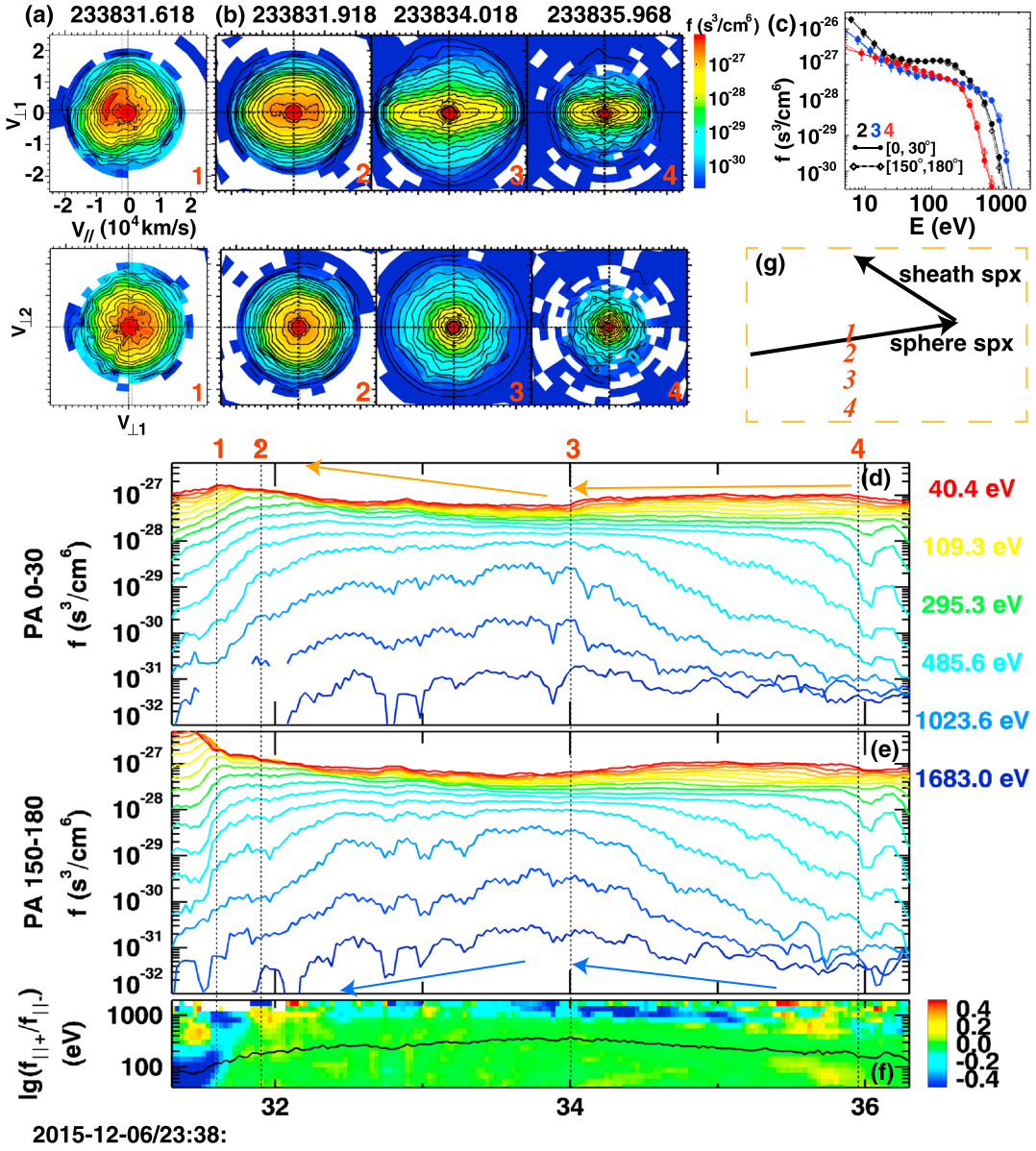

Figure 2. (a) Electron distributions in the $v_{\parallel} - v_{\perp 1}$ and $v_{\perp 1} - v_{\perp 2}$ planes for location 1, where $v_{\perp 1}$ is along $\hat{b}\times\left(\hat{b}\times\hat{v}\right)$, $v_{\perp 2}$ is along $\hat{b}\times\hat{v}$, and $\hat{v}$ is the bulk velocity direction. (b) Distributions for locations 2–4. The center time of each distribution is indicated at the top of each panel (Figures 2a and 2b). (c) 1-D field-aligned distributions for locations 2–4. (d and e) 40–2000 eV parallel and antiparallel electron phase-space densities, with selected energy channel centers listed on the right. Fluxes for low-energy electrons (below ~300 eV) decrease toward the peak $T_{e//}$ location 3, while those for high-energy electrons (~300 to 2000 eV) increase toward the $T_{e//}$ peak. (f) Ratio between the parallel and antiparallel fluxes, roughly balanced in the magnetopsheric inflow region (2–4). Black curve: $T_{e//}$ for <2 keV electrons. Data in Figures 2b–2f are accumulated over five time frames to reduce the statistical uncertainties (overplotted in Figure 2c). (g) Illustration of locations 1–4 relative to the separatrices (black arrows showing magnetic field directions).

remains constant over time (orange arrows illustrate this trend), with a slight decrease barely more significant than the statistical uncertainties (Figure 2c). The trend of increasing $T_{e\|}$ with increasing n and decreasing B is consistent with the parallel potential heating for magnetospheric electrons in the magnetospheric inflow region demonstrated in previous 2-D simulation studies [*Egedal et al.*, 2011]. In terms of the distribution features, the consistency is in the aspect that the density and parallel temperature are increased by addition of high-energy heated magnetospheric electrons, implying that these electrons originate far from

the X line and are energized by the parallel potential along their trajectories, and the parallel potential depth increases toward the separatrix. However, we also notice the following features in the interval 4 to 3 that are not quite consistent with the existing parallel potential heating prediction from 2-D PIC simulation: (1) below the shoulder energy, *f* decreases with energies, deviating from the simulation prediction of a flat-topped distribution [e.g., *Egedal et al.*, 2010]. (2) $T_{e\perp}$ increases from 4 to 3, which can be seen from the blue curve in Figure 1c and the perpendicular thermal spread in distributions in Figure 2b, and it is inconsistent with the μ conservation since *B* decreases.

Locations 3 to 2 mark the region where the $T_{e||}$ and *n* variation trends are inconsistent with the scaling law. As $T_{e||}$ decreases, low-energy *f* increases and high-energy *f* decreases. If the distribution and the shoulder energy are still controlled only by the parallel potential, the decrease of high-energy *f* implies a decreasing depth of the parallel potential toward the separatrix. Previous 2-D PIC simulations [e.g., *Egedal et al.*, 2011] did not show such a variation of $\Phi_{||}$. In the magnetospheric inflow region beyond access of exhaust electrons via the finite gyroradius effect, 2-D simulations predicted that *f* at energies below the shoulder energy does not change, even though the shoulder energy changes with $\Phi_{||}$, inconsistent with the observation. Because of the decrease of the high-energy *f*, the increase of low-energy electrons is associated with the increase of the density and the decrease of $T_{e||}$ for the whole distribution.

The additional low-energy electrons may come from the magnetosheath during the ongoing reconnection due to transport by wave fluctuations in the lower hybrid frequency range. The broadband waves propagating mainly in the out-of-plane direction in the lower hybrid frequency range (as shown in the wave power spectrogram in *Khotyaintsev et al.* [2016]) might be one possible cause for their penetration to the magnetospheric inflow region, as discussed in *Khotyaintsev et al.* [2016] with observations and *Le et al.* [2017] with 3-D simulations. The time domain electric field data are shown in Figure 1f, and intense fluctuations in the intervals 2–3 are observed. Since lower hybrid turbulence could exist near the magnetospheric separatrix both close to the X line and at least tens of d_i downstream [e.g., *Price et al.*, 2016], magnetosheath electrons that penetrate to the magnetospheric inflow region at varying distances from the X line may experience varying degrees of acceleration by the parallel potential. Electrons crossing to the magnetospheric side close to the observation location may not be much energized, because they do not experience a significant parallel potential drop. The decreasing $T_{e||}$ with increasing amounts of low-energy electrons suggests that many newly penetrated magnetosheath electrons enter the magnetospheric inflow region not far from the observation location and are not as efficiently heated by the parallel potential as magnetospheric electrons, causing the total $T_{e||}$ to violate the scaling law of equation (1).

Note that although $T_{e||}$ continues to decrease from locations 2 to 1, it is not considered as a violation of the scaling law. Nongyrotropic outflowing magnetosheath electrons with small $v_{||} < 0$ exist between 1 and 2, and their increasing *f* toward the midplane leads to $T_{e||}$ decrease. The existence of nongyrotropic outflowing magnetosheath electrons suggests that the spacecraft was close to the separatrix region within the scale of magnetosheath electron Larmor radii (illustrated in Figure 2g). Such a $T_{e||}$ decreasing layer with finite Larmor radius effects also exists in 2-D PIC simulations, e.g., the separatrix region with the bulk V_{eL} away from the X line and reduced $T_{e||}$ shown in Figure 2 in *Chen et al.* [2016]. Thus, even in 2-D reconnection, the $T_{e||}$ scaling law does not apply to such a boundary layer, and this region is not considered as a violation of the scaling law.

3.2. Event on 30 October 2015

Figure 3 shows another example where $T_{e||}$ decreases with increasing densities toward the separatrix in the magnetospheric inflow region. This event has been analyzed in *Graham et al.* [2016a], and the parallel heating of electrons was attributed to the parallel potential heating mechanism. Just like event 1, $T_{e||}$ decreases with increasing densities toward the separatrix between locations B and C (Figures 3e and 3f), coexisting with wave fluctuations (Figures 3i and 3j). The spacecraft crossed on −L side of the X line. Starting from location D, the distribution (Figure 3k) is a superposition of antiparallel outflowing magnetosheath electrons and parallel inflowing electrons from the magnetospheric inflow region that extend to higher energies. Thus, the spacecraft is inferred to be on the exhaust side of the separatrix, with a net $V_{eL} < 0$ (Figure 3g), higher antiparallel *f* at low energies (below 100 eV) and higher parallel *f* at high energies (above 100 eV) (Figure 3d). The first time such distribution features occur is one time frame after C, while these features repeatedly appear and disappear during the interval between C and D. Thus, the interval between C and D is identified as the separatrix

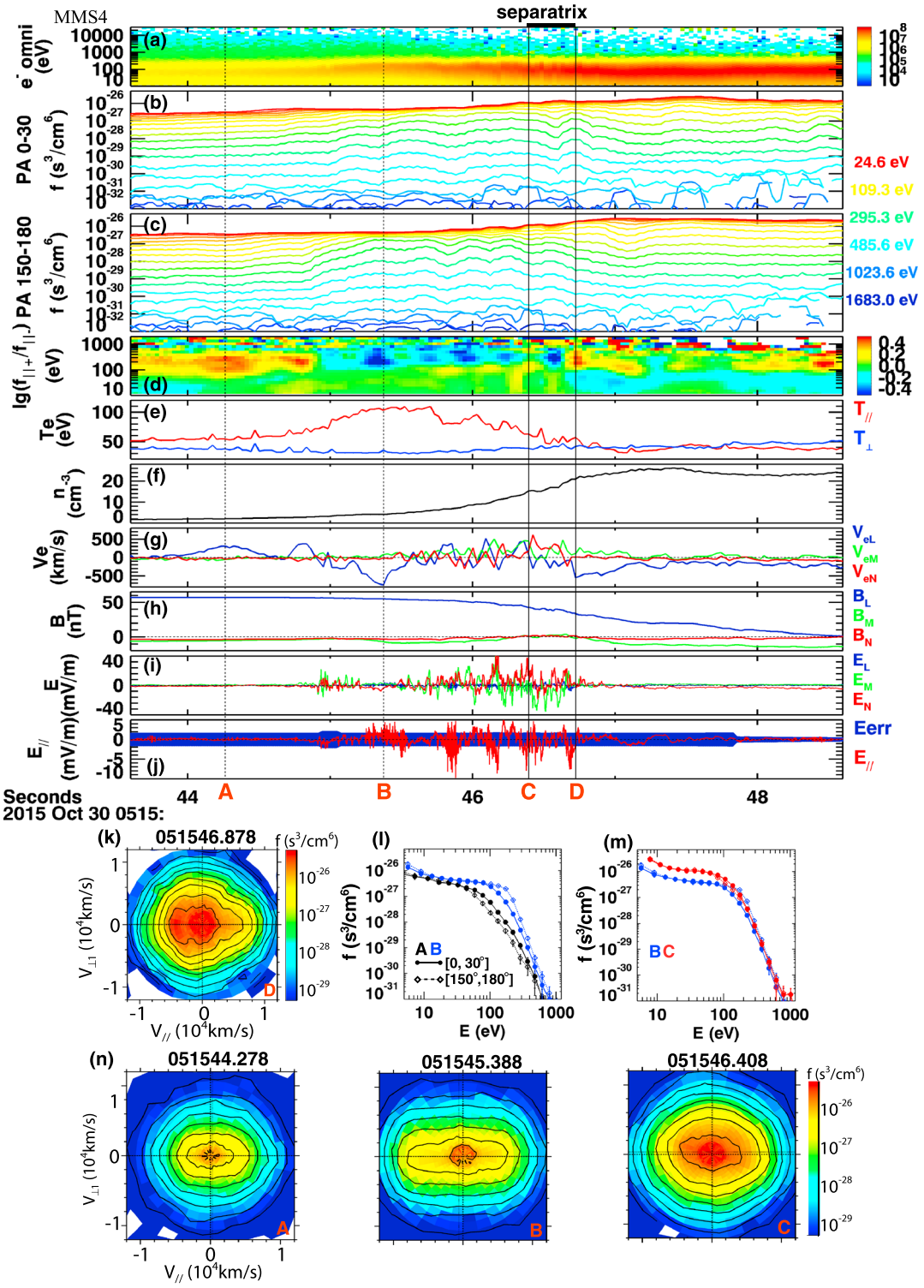

Figure 3. MMS4 crossing of a reconnection region on 30 October 2015. (a) Omni-directional electron energy flux. (b–d) Same formats with Figures 2d–2f. (i and j) The dominant flux direction between the parallel and antiparallel reverses over time for above 100 eV electrons in the magnetospheric inflow region with existence of the electric field fluctuations. (e) Electron temperature with $T_{e//}$ first increases and then decreases at (f) the increasing densities. (g) Electron velocity. (h) Magnetic field. The solid vertical lines mark the separatrix region, with (k) an example of distribution (*D*). (l–n) 1-D and 2-D cuts of distributions in the inflow region.

Table 1. Event List of Electron Parallel Heating in the Magnetospheric Inflow Region Close to the Separatrix, With High-Energy (Hundreds of eV to ~2 keV) Electron Flux Variations That Cannot be Explained by the Typical Parallel Potential Alone[a]

No.	UT (Yyyymmdd-Hhmm)	cot cot(θ_B/2)	(2.1)	(2.2)
1	20151006-1518	0.47	Y	–
2	20151008-0948	0.30	Y	–
3	20151018-1512	0.19	–	Fluctuations
4	20151023-1527	0.22	Y*	Fluctuations
5	20151030-0515	0.46	–	Reversals
6	20151101-1508	0.29	–	Fluctuations
7	20151111-1235	0.21	–	Reversals
8	20151119-1041	0.96	–	Reversals
9	20151205-2339	0.15	–	Reversals
10	20151206-2338	0.25	Y	–
11	20151208-0006	0.14	Y	–
12	20151208-1120	0.36	–	Reversals
13	20151211-1216	0.38	–	Fluctuations
14	20151212-0003	0.19	Y	–
15	20151213-0041	0.72	Y	–
16	20151214-0117	0.41	–	Reversals
17	20151214-2254	0.11	–	Reversals
18	20160104-0111	0.76	–	Reversals
19	20160204-2125	0.19	Y	–
20	20160222-2314	0.41	–	Reversals

[a]cot cot(θ_B/2): cotangent of half the magnetic field shear angle, representing the guide field level relative to the reconnecting component (2.1): Feature (2.1) listed in section 4. Existence of an interval of increasing high-energy fluxes with increasing $T_{e||}$ and decreasing total densities, where parallel and antiparallel fluxes are balanced ("Y") or with higher fluxes toward the reconnection site as expected in the inflow region ("Y*") (2.2): Feature (2.2) in section 4. Existence of asymmetric high-energy flux fluctuations between the parallel and antiparallel directions, with ("Reversals") or without ("Fluctuations") reversals of their ratios over time.

region. The spacecraft is inferred to be in the magnetospheric inflow region before C, and the regions B and C also violates the $T_{e||}$ scaling law (equation (1)). Based on the timing analysis reported in *Graham et al.* [2016a], the length scale between locations B and C corresponds to about 0.7 d_i.

The most prominent difference between this event and the first one is that high $V_{||}$ phase-space densities are imbalanced and the dominant side ($V_{||} > 0$ or $V_{||} < 0$) switches (Figures 3b–3d). Since the spacecraft is on the −L side of the X line and in the magnetospheric inflow region, according to the Hall current structure predicted by 2-D simulations, f in the direction toward the X line (parallel in this case) may be slightly higher than that in the opposite direction, leading a bulk velocity toward the X line ($V_{eL} > 0$) [e.g., *Chen et al.*, 2016, Figure 2d]. Such imbalance is observed at location A (red color in Figure 3d). However, the imbalance unexpectedly changes to be dominant in the antiparallel direction around 05:15:45–05:15:46.5 UT (blue color in Figure 3d). Figure 3l plots examples of 1-D distributions at locations A and B to show the imbalance in f. 2-D cuts of distributions for A–C are shown in Figure 3n. The imbalance during A–C is not negligible, as the ratio $f_{||+}/f_{||-}$ is greater than 2 or less than 1/2, which leads to a current density along L up to 1.4 μA/m^2 and alters the Hall current and field pattern. Figure 3m shows 1-D distributions at locations B and C. As $T_{e||}$ generally decreases from B to C, the major change in distributions is the increase of low-energy f; high-energy f fluctuates, leading to small-amplitude $T_{e||}$ variations. In short, although distributions B and C are quasi-flat-top (above 10 eV), discrepancies of electron heating features from the parallel potential mechanism lie in the decreasing $T_{e||}$ trend, increase of low-energy f rather than high-energy f, and the field-aligned distribution imbalance with reversals of the direction with dominant f.

4. Summary

In this study, we have analyzed the parallel heating for gyrotropic electrons below ~2 keV in the magnetospheric inflow region near the separatrix. As demonstrated by the two events shown above, in a subregion of the inflow close to the separatrix, $T_{e||}$ decreases toward the separatrix with increasing densities, and thus, the adiabatic $T_{e||}$ scaling law (equation (1)) is violated. Such $T_{e||}$ variation cannot be explained by the heating mechanism of the parallel potential for magnetospheric electrons that were shown in two-dimensional simulations alone [e.g., *Egedal et al.*, 2011]. Broadband electromagnetic wave fluctuations in the lower hybrid frequency range exist in this subregion. Further in the magnetospheric inflow region, the trend of $T_{e||}$, density, and high-energy f variations agree with the parallel potential mechanism prediction, while the distribution shape and $T_{e\perp}$ variation still exhibit noticeable differences from the parallel potential theory.

Corresponding distribution features along the decreasing $T_{e||}$ toward the separatrix include the following: (1) more low-energy (below ~300 eV) electrons are mixed in. (2) High-energy electron (a few hundred eV to

~2 keV) distributions may either (2.1) exhibit the same trend with $T_{e||}$ with quasi-balanced distributions between the parallel and antiparallel directions (e.g., 2015–12-06 event) or (2.2) exhibit fluctuating phase-space densities that are imbalanced between the parallel and antiparallel directions, where the direction with dominant fluxes may reverse over time (e.g., 30 October 2015 event).

Based on our investigation of MMS observations during the first dayside magnetopause season (September 2015 to March 2016), the subregion of decreasing $T_{e||}$ and increasing densities with gyrotropic magnetosheath-like electrons is commonly observed. Twenty events are listed in Table 1 as examples, and electron heating and distribution features are briefly described. The subregion extends further to the magnetospheric side than the separatrix region on the scale of order d_i. There are 8/20 events with feature (2.1) and 13/20 events with feature (2.2). The event base spans a range of the guide field level of about 0.1 to 1 of the reconnecting component, suggesting that the existence of such a subregion is insensitive to the guide field strength. Here the guide field level is estimated by the cotangent of half magnetic field shear angles between the magnetosheath and magnetosphere ($\cot\cot(\theta_B/2)$), equivalent to $|B_M/B_L|$ assuming that the X line is along the bisection between the upstream magnetic fields [*Hesse et al.*, 2013].

5. Discussions

The above summarized features in the $T_{e||}$ decrease subregion may be related to wave activities near the separatrix region, e.g., in the lower hybrid frequency range. The addition of low-energy electrons could be due to waves transporting magnetosheath electrons to the magnetospheric inflow region. The energization by the parallel potential mechanism depends on the parallel potential drop along the trajectory. If the transport location of magnetosheath electrons is close to the observation location, the parallel potential drop experienced by these penetrated magnetosheath electrons along the magnetic field in the magnetospheric inflow region would be small, and these electrons cannot obtain as much energy as magnetospheric origin electrons from far upstream. *Graham et al.* [2016b] estimated that the diffusion coefficient of lower hybrid waves is strong enough to enable penetration of magnetosheath electrons to the magnetospheric inflow region and pointed out that the parallel electron heating cannot be explained by trapping of magnetospheric electrons by the parallel potential alone.

If the parallel potential is the only heating mechanism, decreasing f at high energies toward the separatrix (like in event 1) indicates decreasing depth of the parallel potential. The penetration of low-energy electrons may be one factor to change the parallel potential structure. As shown in 2-D symmetric simulations, $E_{||}$ in the inflow region is mainly supported by the electron parallel pressure gradient along magnetic fields [*Haggerty et al.*, 2015]. Thus, addition of low-energy electrons may reduce the field-aligned pressure gradient and $E_{||}$, leading to shallower parallel potential depth close to the separatrix. Consequently, the upper energy limit (the shoulder energy of a distribution) for trapped and heated magnetospheric electrons decreases, so does the high-energy f. Further work is needed for detailed analysis on whether and how the parallel potential structure would be modified.

In addition to allowing magnetosheath electron transport, wave-particle interaction may produce parallel acceleration/deceleration, as another possible mechanism to change high-energy distributions besides the parallel potential structure modification. For example, obliquely propagating waves with $E_{||}$ fluctuations may lead to Landau resonance with electrons, producing distributions with a shoulder extending to parallel phase velocities [*Cairns and McMillan*, 2005]. The resonance depends on the propagation direction and might lead to distributions with imbalanced f between the parallel and antiparallel directions. Existence of significant $E_{||}$ fluctuations for the two events is shown in Figures 1g and 3j. *Graham et al.* [2016a] suggested that lower hybrid waves are much less important than the parallel potential in producing parallel electron heating. However, the wave analysis therein was based on perpendicular electric fields, and the possibility of Landau resonance with $E_{||}$ is yet to be explored. Distributions with significant anisotropy may excite instabilities, which in turn reduce the anisotropy [e.g., *Gary and Nishimura*, 2003]. The magnetospheric inflow region has low electron β ($\beta_{e||} < 1$ for the presented two events), so wave excitation due to the fluid electron firehose instability that requires $\beta_{e||} > 2$ is ruled out. The condition for kinetic electron firehose instability $T_{e\perp}/T_{e||} < 1 - S/\beta_{e||}^{\alpha}$ is also far from satisfaction, where S and α are constants according to the linear theory and simulation results [e.g., *Gary and Nishimura*, 2003]. It is still an open question whether some type of wave-particle

interactions other than the firehose instability could cause the continuous $T_{e||}$ decrease toward the separatrix. The effect of waves will be quantitatively studied in future work.

Acknowledgments
The research is supported in part by NSF grants AGS-1543598, AGS-1202537, AGS-1552142, DOE grant DESC0016278 and NASA grants to the MMS Theory and Modeling and FPI at GSFC. IRAP contribution to MMS was supported by CNES and CNRS. MMS data are available at MMS Science Data Center (https://lasp.colorado.edu/mms/sdc/public/). The SPEDAS software used for data analysis in this paper is available at http://themis.ssl.berkeley.edu/socware/bleeding_edge/.

References

Bessho, N., L.-J. Chen, K. Germaschewski, and A. Bhattacharjee (2015), Electron acceleration by parallel and perpendicular electric fields during magnetic reconnection without guide field, *J. Geophys. Res. Space Physics*, *120*, 9355–9367, doi:10.1002/2015JA021548.

Bessho, N., L.-J. Chen, and M. Hesse (2016), Electron distribution functions in the diffusion region of asymmetric magnetic reconnection, *Geophys. Res. Lett.*, *43*, 1828–1836, doi:10.1002/2016GL067886.

Cairns, I. H., and B. F. McMillan (2005), Electron acceleration by lower hybrid waves in magnetic reconnection regions, *Phys. Plasmas*, *12*, 102110, doi:10.1063/1.2080567.

Chen, L.-J., et al. (2008), Evidence of an extended electron current sheet and its neighboring magnetic island during magnetotail reconnection, *J. Geophys. Res.*, *113*, A12213, doi:10.1029/2008JA013385.

Chen, L.-J., M. Hesse, S. Wang, N. Bessho, and W. Daughton (2016), Electron energization and structure of the diffusion region during asymmetric reconnection, *Geophys. Res. Lett.*, *43*, 2405–2412, doi:10.1002/2016GL068243.

Egedal, J., W. Daughton, J. F. Drake, N. Katz, and A. Le (2009), Formation of a localized acceleration potential during magnetic reconnection with a guide field, *Phys. Plasmas*, *16*(5), doi:10.1063/1.3130732.

Egedal, J., A. Lê, N. Katz, L.-J. Chen, B. Lefebvre, W. Daughton, and A. Fazakerley (2010), Cluster observations of bidirectional beams caused by electron trapping during antiparallel reconnection, *J. Geophys. Res.*, *115*, A03214, doi:10.1029/2009JA014650.

Egedal, J., A. Le, P. L. Pritchett, and W. Daughton (2011), Electron dynamics in two-dimensional asymmetric anti-parallel reconnection, *Phys. Plasmas*, *18*, 102901, doi:10.1063/1.3646316.

Gary, S. P., and K. Nishimura (2003), Resonant electron firehose instability: Particle-in-cell simulations, *Phys. Plasmas*, *10*, 3571–3576, doi:10.1063/1.1590982.

Graham, D. B., et al. (2016a), Electron currents and heating in the ion diffusion region of asymmetric reconnection, *Geophys. Res. Lett.*, *43*, 4691–4700, doi:10.1002/2016GL068613.

Graham, D. B., et al. (2016b), Lower hybrid waves in the ion diffusion and magnetospheric inflow regions, *J. Geophys. Res. Space Physics*, *122*, 517–533, doi:10.1002/2016JA023572.

Haggerty, C. C., M. A. Shay, J. F. Drake, T. D. Phan, and C. T. McHugh (2015), The competition of electron and ion heating during magnetic reconnection, *Geophys. Res. Lett.*, *42*, 9657–9665, doi:10.1002/2015GL065961.

Hesse, M., N. Aunai, S. Zenitani, M. Kuznetsova, and J. Birn (2013), Aspects of collisionless magnetic reconnection in asymmetric systems, *Phys. Plasmas*, *20*(6), 061210, doi:10.1063/1.4811467.

Khotyaintsev, Y. V., et al. (2016), Electron jet of asymmetric reconnection, *Geophys. Res. Lett.*, *43*, 5571–5580, doi:10.1002/2016GL069064.

Lavraud, B., et al. (2016), Currents and associated electron scattering and bouncing near the diffusion region at Earth's magnetopause, *Geophys. Res. Lett.*, *43*, 3042–3050, doi:10.1002/2016GL068359.

Le, A., J. Egedal, W. Daughton, W. Fox, and N. Katz (2009), Equations of state for collisionless guide-field reconnection, *Phys. Rev. Lett.*, *102*, 085001, doi:10.1103/PhysRevLett.102.085001.

Le, A., W. S. Daughton, L.-J. Chen, and J. Egedal (2017), Enhanced electron mixing and heating in 3D asymmetric reconnection at the Earth's magnetopause, *Geophys. Res. Lett.*, *44*, 2096–2104, doi:10.1002/2017GL072522.

Le Contel, O., et al. (2016), Whistler mode waves and Hall fields detected by MMS during a dayside magnetopause crossing, *Geophys. Res. Lett.*, *43*, 5943–5952, doi:10.1002/2016GL068968.

Phan, T. D., et al. (2016), Ion Larmor radius effects near a reconnection X line at the magnetopause: THEMIS observations and simulation comparison, *Geophys. Res. Lett.*, *43*, 8844–8852, doi:10.1002/2016GL070224.

Pollock, C., et al. (2016), Fast plasma investigation for magnetospheric multiscale, *Space Sci. Rev.*, *199*, 331–406, doi:10.1007/s11214-016-0245-4.

Price, L., M. Swisdak, J. F. Drake, P. A. Cassak, J. T. Dahlin, and R. E. Ergun (2016), The effects of turbulence on three-dimensional magnetic reconnection at the magnetopause, *Geophys. Res. Lett.*, *43*, 6020–6027, doi:10.1002/2016GL069578.

Russell, C. T., et al. (2016), The Magnetospheric Multiscale Magnetometers, *Space Sci. Rev.*, *199*, 189–256, doi:10.1007/s11214-014-0057-3.

Shay, M. A., T. D. Phan, C. C. Haggerty, M. Fujimoto, J. F. Drake, K. Malakit, P. A. Cassak, and M. Swisdak (2016), Kinetic signatures of the region surrounding the X line in asymmetric (magnetopause) reconnection, *Geophys. Res. Lett.*, *43*, 4145–4154, doi:10.1002/2016GL069034.

Torbert, R. B., et al. (2014), The FIELDS instrument suite on MMS: Scientific objectives, measurements, and data products, *Space Sci. Rev.*, doi:10.1007/s11214-014-0109-8.